Cell, Vol. 104, 205–215, January 26, 2001, Copyright ©2001 by Cell Press

Loss of the ClC-7 Chloride Channel Leads to Osteopetrosis in Mice and Man

Uwe Kornak,*‖# Dagmar Kasper,*‖
Michael R. Bösl,* Edelgard Kaiser,†
Michaela Schweizer,* Ansgar Schulz,‡
Wilhelm Friedrich,‡ Günter Delling,†
and Thomas J. Jentsch*§
*Zentrum für Molekulare Neurobiologie Hamburg
ZMNH
Universität Hamburg
D-20246 Hamburg
Germany
†Abteilung für Osteopathologie
Pathologisches Institut
Universität Hamburg
D-20246 Hamburg
Germany
‡Universitätskinderklinik
Universität Ulm
D-89075 Ulm
Germany

Summary

Chloride channels play important roles in the plasma membrane and in intracellular organelles. Mice deficient for the ubiquitously expressed ClC-7 Cl^- channel show severe osteopetrosis and retinal degeneration. Although osteoclasts are present in normal numbers, they fail to resorb bone because they cannot acidify the extracellular resorption lacuna. ClC-7 resides in late endosomal and lysosomal compartments. In osteoclasts, it is highly expressed in the ruffled membrane, formed by the fusion of H^+-ATPase-containing vesicles, that secretes protons into the lacuna. We also identified *CLCN7* mutations in a patient with human infantile malignant osteopetrosis. We conclude that ClC-7 provides the chloride conductance required for an efficient proton pumping by the H^+-ATPase of the osteoclast ruffled membrane.

Introduction

Chloride channels of the CLC gene family reside in the plasma membrane and in intracellular organelles. Their various functions are illuminated by diseases that are caused by mutations in three of the nine known mammalian CLC genes (Jentsch et al., 1999). Mutations in the muscle Cl^- channel ClC-1 lead to myotonia (Steinmeyer et al., 1991), highlighting its importance in stabilizing the membrane potential of muscle. Mutations in the kidney-specific ClC-Kb cause a form of Bartter's syndrome (Simon et al., 1997), indicating a role in transepithelial transport. Finally, mutations of ClC-5 cause Dent's disease (Lloyd et al., 1996), a disorder characterized by proteinuria and kidney stones.

In contrast to plasma membrane channels like ClC-1 or ClC-Kb, ClC-5 functions in intracellular membranes. ClC-5 is present in endosomes of the renal proximal tubule where it colocalizes with the proton pump and endocytosed protein (Günther et al., 1998). The disruption of ClC-5 in mice entails a defect in proximal tubular endocytosis (Piwon et al., 2000) that probably results from an impairment of endosomal acidification.

Several other CLC channels also reside in intracellular membranes. ClC-3 and ClC-4 are close homologs of ClC-5 and form a branch of the gene family that is most closely related to the single yeast CLC gene *GEF1*. Gef1p resides in a late Golgi compartment where it may provide an electrical shunt necessary for an efficient operation of the proton ATPase (Gaxiola et al., 1998; Schwappach et al., 1998). Indeed, disruption of the *VMA3* subunit of the yeast V-type ATPase or of *GEF1* gave a common phenotype (Greene et al., 1993). Recently, we discovered that ClC-3 is present in endosomes and synaptic vesicles where it contributes to their acidification (Stobrawa et al., 2001[January issue of *Neuron*]).

Much less is known about the third branch of the CLC family, which comprises ClC-6 and ClC-7 (Brandt and Jentsch, 1995). Both genes are already transcribed early in development and are nearly ubiquitously expressed in adults. No plasma membrane currents were detected upon heterologous expression of either protein in *Xenopus* oocytes, possibly indicating an intracellular localization. The physiological function of either channel has remained obscure.

Many intracellular compartments, including vesicles of endosomal and secretory pathways, are acidified by V-type proton ATPases. Vesicular acidification is important for luminal enzymatic activities, proton-coupled transport processes, receptor–ligand interactions, sorting, and vesicle trafficking. For efficient operation, the electrogenic proton pump needs a parallel conductance that shunts its electric current. In most vesicles, this conductance is selective for chloride (al-Awqati, 1995). Some specialized cells use regulated exocytosis to insert vesicular proton pumps into the plasma membrane in order to acidify extracellular compartments. This includes osteoclasts, multinucleated cells responsible for bone resorption (Väänänen et al., 2000). After attaching to the bone matrix, osteoclasts undergo polarization and form a special membrane facing the bone (the "ruffled border") by the fusion of acidic intracellular vesicles containing proton pumps (Baron et al., 1985; Blair et al., 1989). The exocytotic delivery of acid and proteases, as well as a direct transport of acid across the ruffled border, is needed to dissolve bone material in the tightly sealed resorption lacuna between the osteoclast and the bone. The low pH of this "extracellular lysosome" is crucial for the solubilization of inorganic bone material and the digestion of the organic matrix by acid hydrolases. To ensure electroneutrality of acid secretion, the ruffled border contains Cl^- channels that are inserted

§To whom correspondence should be addressed (e-mail: jentsch@plexus.uke.uni-hamburg.de).
‖These authors contributed equally to this work.
#Ph.D. student of the Faculty for Biology, Chemistry, and Pharmacy of the Freie Universität Berlin.

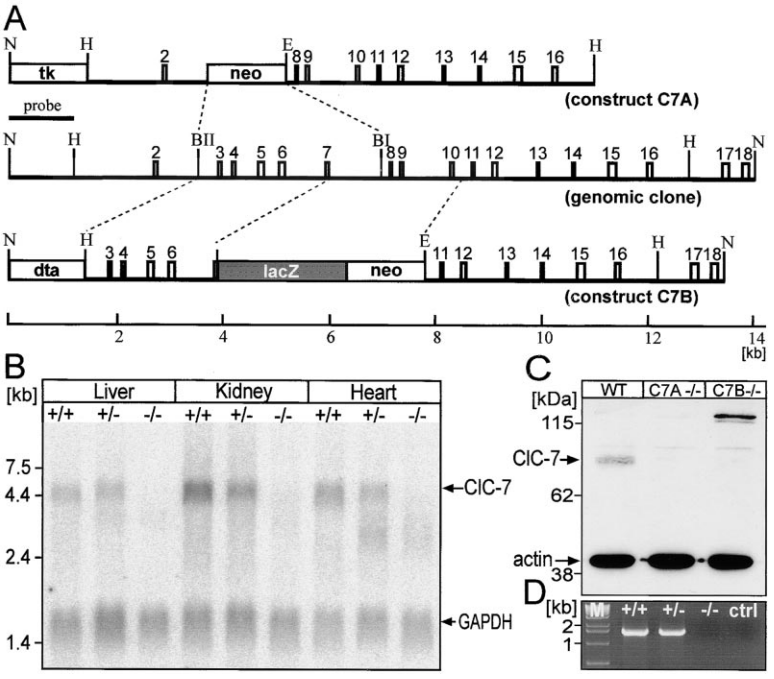

Figure 1. Disruption of the *Clcn7* Gene

(A) Targeting of the *Clcn7* gene. The top shows construct C7A (neo: neomycin resistance cassette; tk: thymidine kinase cassette). A genomic clone with exons 2–18 (boxes) and important restriction sites (BII = BglII, BI = BsrGI, E = EcoRI, H = HinDIII, N = NotI) is shown below (Kornak et al., 1999). In the targeting vector C7B (bottom), a lacZ/neomycin cassette was inserted in frame into exon 7 (dta: diphtheria toxin α fragment cassette).

(B) Northern blot of poly(A)$^+$ RNA from various tissues of +/+, +/−, and −/− animals from the C7B strain, using a 3′ ClC-7 cDNA probe and a GAPDH probe as control. A ClC-7-specific band of ~4.4 kb is absent from *Clcn7*$^{-/-}$ tissues.

(C) Western blot of lysates from embryonic fibroblasts using the amino-terminal ClC-7 antibody 11753. The ~80 kDa ClC-7 protein is absent in strain C7A. The ~130 kDa band in strain C7B represents the ClC-7/β-galactosidase fusion protein. Actin staining (below) was used as control.

(D) RT-PCR on RNA from C7A fibroblasts. No PCR product is observed in the −/− lane, nor in the negative control (Ctrl). M: marker.

by exocytotic fusion together with the H^+-ATPase. The molecular identity of these channels has not yet been established.

Mutations in two human genes are known to cause osteopetrosis by impairing osteoclast function. Both genes are important for proton secretion. Carbonic anhydrase II deficiency leads to a relatively mild osteopetrosis associated with renal tubular acidosis (Sly et al., 1983). This enzyme generates carbonic acid, which supplies the H^+-ATPase with its substrate. Mutations in the a3 subunit of the osteoclast H^+-ATPase are a frequent cause of infantile malignant osteopetrosis (Frattini et al., 2000; Kornak et al., 2000). A spontaneous mutation in the corresponding gene in the osteosclerotic (*oc*) mouse, as well as its disruption by homologous recombination, lead to a similar phenotype in mice (Li et al., 1999; Scimeca et al., 2000).

We now show that ClC-7 is a late endosomal/lysosomal Cl^- channel that is highly expressed in osteoclasts where it can be inserted into the ruffled border. Disruption of ClC-7 in mice led to severe osteopetrosis that was due to a failure of osteoclasts to secrete acid. As observed in some patients suffering from malignant infantile osteopetrosis, *Clcn7*$^{-/-}$ mice additionally developed severe retinal degeneration. Testing *CLCN7* as a candidate gene for the human disease, we identified a child with malignant osteopetrosis who was a compound heterozygote for *CLCN7* mutations. Our work reveals *CLCN7* as a novel gene underlying human osteopetrosis and demonstrates that it encodes the long-sought Cl^- channel involved in osteoclast HCl secretion. The expression pattern of ClC-7 and the degeneration of the retina suggest that it may play an important role in intracellular compartments of neuronal and other tissues as well.

Results

Disruption of the *Clcn7* Gene

We used two different strategies to disrupt the *Clcn7* gene (Figure 1A). Construct C7A was designed to abolish expression of ClC-7 completely, whereas in construct C7B, a lacZ reporter gene was fused in frame to exon 7. This should result in a fusion protein between the NH_2-terminal part of ClC-7 (up to transmembrane domain D2) and β-galactosidase. Embryonic stem cells targeted by either construct were used to generate two independent mouse strains (termed C7A and C7B, respectively). Northern blot and RT-PCR analysis confirmed that normal ClC-7 mRNA was absent from *Clcn7*$^{-/-}$ mice of either strain (Figures 1B and 1D). Western blot analysis using an antibody directed against the ClC-7 amino-terminus revealed that this protein is absent from *Clcn7*$^{-/-}$ fibroblasts of strain C7A (Figure 1C). The 130 kDa band detected in C7B mice represents the ClC-7/β-galactosidase fusion protein.

Embryonic Tissue Distribution and Subcellular Localization of ClC-7

ClC-7 is already expressed during early embryogenesis (Brandt and Jentsch, 1995). Although ClC-7 disruption did not seem to affect prenatal development, we investigated the expression of ClC-7 at embryonic day E16.5 by in situ hybridization (Figures 2A and 2B) and X-Gal staining using strain C7B (Figures 2C–2F). There was a ubiquitous weak basal expression. Both techniques revealed a prominent staining of dorsal root ganglia (DRG), the trigeminal ganglion, the eye, and brain. These signals were specific as they were absent in knockout (KO) animals (in situ hybridization; Figure 2B) or in wild-type (WT) animals (X-Gal staining; Figure 2C), respec-

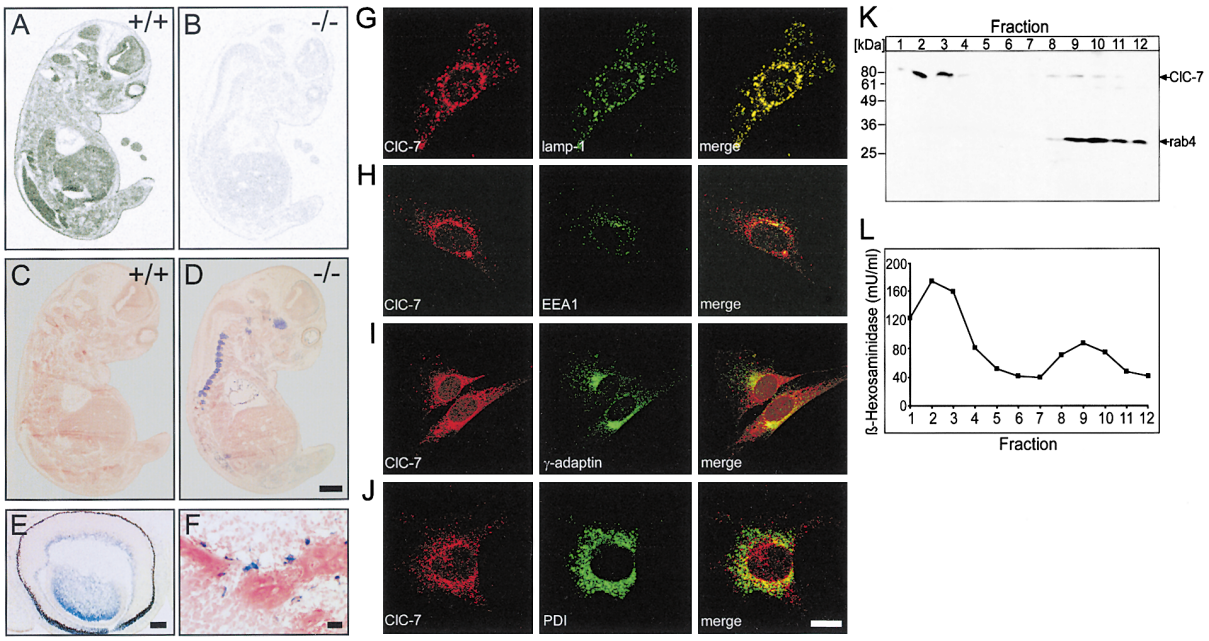

Figure 2. Tissue Distribution and Subcellular Localization of ClC-7

(A and B) In situ hybridization of WT (A) and KO (B) E16.5 embryos with a ClC-7 antisense probe. Prominent staining was present in WT dorsal root ganglia, trigeminal ganglion, spinal cord, brain, and eye. Signals were absent in the *Clcn7*$^{-/-}$ embryo. (C–F) Cryosections of E16.5 embryos stained with X-Gal and eosin. (C) No staining was visible in WT. (D) *Clcn7*$^{-/-}$ embryo (strain C7B) shows intense blue staining in dorsal root ganglia, trigeminal ganglion, frontal brain, and eye. (E) X-Gal stained eye of *Clcn7*$^{-/-}$ embryo. ClC-7 is expressed in the lens, the retinal pigment epithelium, and cells of the neuroretina. This is also true for neonatal animals (not shown). (F) Bone trabecula surrounded by X-Gal-positive osteoclasts in the KO embryo. (G–J) Colocalization by immunofluorescence of ClC-7 (red) with intracellular markers (green) in mouse fibroblasts (MF). (G) Nearly all ClC-7-positive vesicles stained for lamp-1, suggesting a late endosomal to lysosomal localization. ClC-7 colocalized poorly with the following markers: (H) early endosome antigen (EEA1), (I) γ-adaptin (a trans-Golgi network marker), (J) protein disulfide isomerase (PDI) (an ER marker). (K and L) Cell fractionation of mouse fibroblasts. (K) Western analysis of ClC-7 and early endosome marker rab4. ClC-7 is mainly present in lysosomal fractions 2 and 3, but also in endosomal fractions 8 to 10 where it copurifies with rab4. (L) Activity of the lysosomal enzyme β-hexosaminidase. Scale bars: (A–D) 1mm; (E and F) 100 μm; (G–J) 50 μm.

tively. *Clcn7* was transcribed in the embryonic lens, neuroretina, and retinal pigment epithelium (RPE) (Figure 2E). Embryonic osteoclasts expressed high levels of the ClC-7/β-galactosidase fusion protein (Figure 2F). Similar, albeit weaker, staining was seen in heterozygous embryos from strain C7B.

The subcellular localization of endogenous ClC-7 protein was determined in mouse embryonic fibroblasts (MF) by immunofluorescence (Figures 2G–2J). ClC-7 was present in vesicular structures throughout the cytoplasm, but could not be detected in the plasma membrane. There was a nearly complete overlap with lamp-1, a protein expressed in late endosomes and lysosomes. Only limited colocalization was observed with early endosome antigen (EEA1), the trans-Golgi network marker γ-adaptin, and with the endoplasmatic reticulum marker protein disulfide isomerase (PDI) (Figures 2H–2J).

These results were confirmed by analyzing membrane fractions of MFs separated by Percoll density centrifugation (Figure 2K). The enzymatic activity of the lysosomal acidic hydrolase β-hexosaminidase copurified with ClC-7 (Figure 2L). ClC-7 and the endosomal marker rab4 overlapped in fractions 8–10, which contained late and early endosomes.

Clcn7$^{-/-}$ Mice Develop Severe Osteopetrosis

Heterozygous *Clcn7*$^{+/-}$ animals were indistinguishable from wild-type (WT) mice, but *Clcn7*$^{-/-}$ (KO) animals of both strains had an identical, severe phenotype. Roughly 25% of E18 embryos from heterozygous matings were *Clcn7*$^{-/-}$. Due to an increased postnatal lethality, this number dropped to ~16% at P7. KO mice were smaller, had dysmorphic heads, an abnormal body posture, and short limbs (Figure 3A). Teeth were formed, but did not erupt. Growth retardation became apparent during the second postnatal week and could not be prevented by feeding liquid diet (Figure 3C). *Clcn7*$^{-/-}$ animals did not survive for more than 6–7 weeks. Radiographs of 4-week-old littermates disclosed details of the dysmorphism (Figure 3B). At higher magnification, radiographs of the tibia (Figure 3D) showed that the shortened long bones of the *Clcn7*$^{-/-}$ mice lacked a marrow cavity. Tibia sections revealed a disorganized trabecular structure, fibrosis, and an absence of a regular corticalis (Figure 3E). Subtle changes in bone morphology were already observable at E16 at sites of beginning mineralization. The ratio of total bone volume to trabecular volume was increased about 7-fold in KO mice at day P42 (Figure 3F). A calcein/tetracycline labeling experiment was used to assess bone apposition rate, which depends on osteoblast function. It was not increased in KO mice (data not shown). Another marker for osteoblast activity is serum levels of alkaline phosphatase (Christenson, 1997). These were elevated in mutant mice (1151 ± 252 U/l (−/−) versus 383 ± 22 U/l (+/+ and +/−) ($n \geq 7$ ± SEM)), probably reflecting the

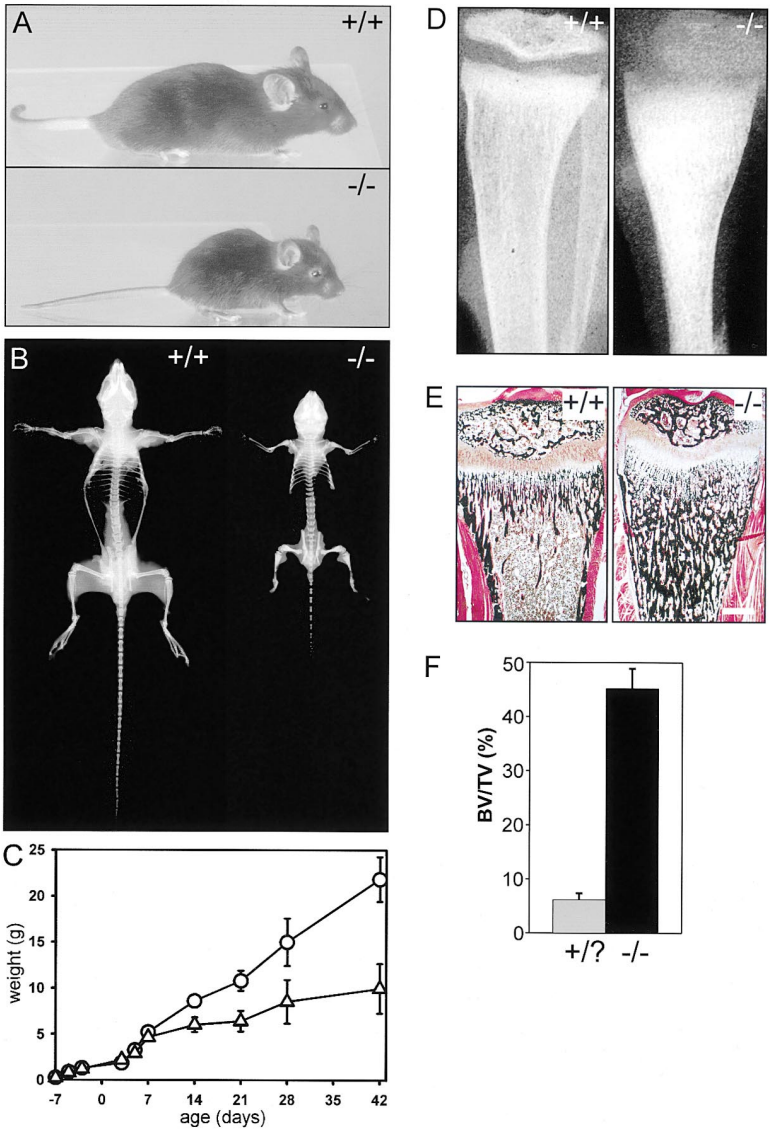

Figure 3. Gross Morphological Changes in *Clcn7*$^{-/-}$ Animals

(A) 4-week-old WT animal (+/+) and a *Clcn7*$^{-/-}$ littermate (−/−).

(B) X-ray of a 4-week-old +/+ mouse and a −/− littermate. No bone marrow cavity is seen in long bones.

(C) Weight of *Clcn7*$^{-/-}$ animals (open triangle) from day E14 (−7) to P42 in comparison to WT and heterozygous mice (open circle) (n ≥ 4).

(D) X-ray and (E) von Kossa staining of +/+ and −/− tibia. No ordered corticalis and no marrow cavity is formed in −/− tibia.

(F) Total bone volume (BV) over trabecular volume (TV) in tibiae. Bone density is increased about 7-fold in −/− mice at day P42 (n = 4). Scale bar: 0.5 mm

increased number of osteoblasts due to the enlarged surface of the osteopetrotic bone. Electrolyte concentrations in serum or urine (including Ca^{2+} and P_i) were not significantly different from WT (data not shown). In osteopetrotic patients, the decrease in bone marrow space often entails extramedullary blood production that causes hepatosplenomegaly (Gerritsen et al., 1994). Likewise, *Clcn7*$^{-/-}$ mice KO mice were anemic (hematocrit: 34 ± 2% (−/−) versus 45 ± 1% (+/+ and +/−)) (n ≥ 4 ±SEM) and displayed splenomegaly (10.1 ± 1.3 mg/g (KO) versus 5.0 ± 1.0 mg/g (WT); organ weight/body weight) (n ≥ 4 ±SEM). Hence, *Clcn7*$^{-/-}$ mice suffer from a lethal form of recessive osteopetrosis.

Osteoclast Morphology and Ruffled Border Localization of ClC-7

Osteopetrosis can be caused by an absence of osteoclasts or by their inability to resorb bone (Lazner et al., 1999). Numerous abnormally elongated osteoclasts were present in bones of KO mice (Figure 4B). They stained for tartrate resistant acid phosphatase (TRAP), a marker for osteoclasts, yet resorption lacunae were absent. Electron microscopy revealed that *Clcn7*$^{-/-}$ osteoclasts developed only rudimentary ruffled border membranes. Broad clear zones, which are indicative of a firm attachment to bone, were often visible (Figure 4D). To examine whether adult osteoclasts express ClC-7 to the same high levels as embryonic osteoclasts (Figure 2F), we used X-Gal to stain tibiae of mice from the β-galactosidase-expressing strain C7B (Figure 4E). The strongest label was again associated with multinucleated osteoclasts attached to the bone surface. Immunohistochemistry using a ClC-7 antibody confirmed this finding (Figures 4F and 4G). Similar to fibroblasts (Figures 2G–2J), all osteoclasts were stained intracellularly. In some cases, the signal was additionally concentrated at the osteoclast/bone interface. To analyze the subcellular distribution of ClC-7 in more detail, we performed double immunofluorescence using antibodies against

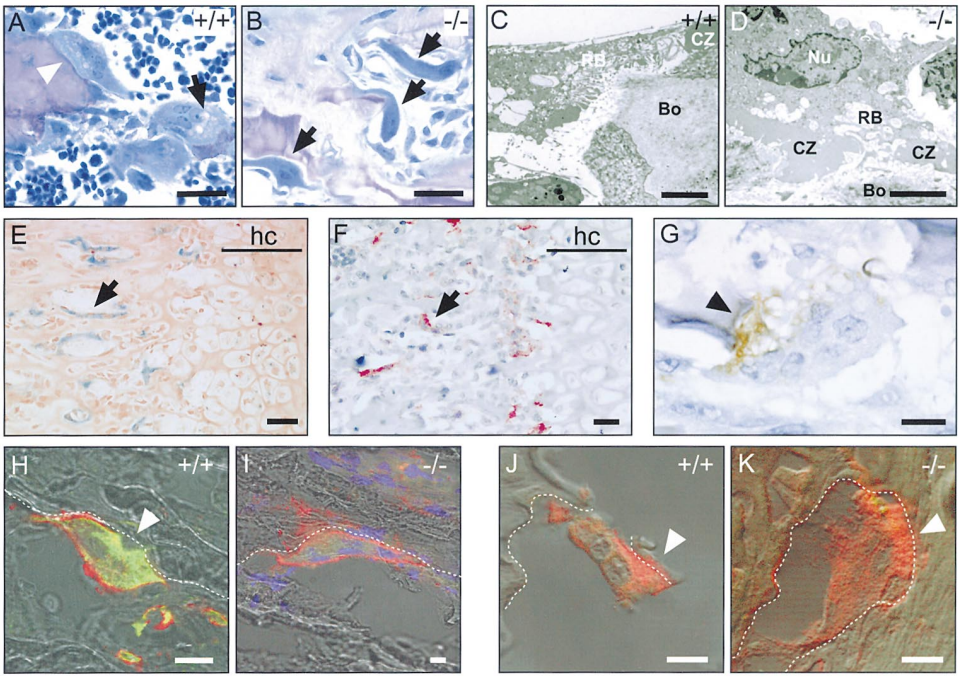

Figure 4. Morphology of Osteoclasts of *Clcn7*$^{-/-}$ Mice and Expression of ClC-7 in Bone Tissue

(A and B) Toluidine blue staining of tibia sections (purple = bone; blue = osteoclasts/stromal cells). Ruffled borders (light blue zone, arrowhead) and large vesicles (arrow) containing degraded bone material are frequently seen in WT osteoclasts (A), but are absent in KO osteoclasts (B) (arrows). (C and D) Electron micrographs of osteoclasts. (C) A ruffled border (RB) is present in a resorbing WT osteoclast. (D) *Clcn7*$^{-/-}$ osteoclasts form only rudimentary ruffled borders (RB) and transcytotic vesicles (Bo = Bone, CZ = Clear Zone, Nu = Nucleus). (E and F) Sections of tibial epiphyseal plate (hc = hypertrophic chondrocytes). (E) X-Gal staining (blue) of a P35 C7B −/− tibia (Kernechtrot counterstaining) labeled multinucleated osteoclasts (arrow). (F) ClC-7 revealed by alkaline phosphatase immunohistochemistry (red). Osteoclasts lining the bone surface (arrow) are stained. (G) ClC-7 expression by horseradish peroxidase immunohistochemistry (brown). A vesicular and a ruffled border staining (arrowhead) can be distinguished. (H and I) Immunofluorescent detection of ClC-7 (green) and β_3-integrin (red) in osteoclasts (dotted lines = bone surface). (H) WT: β_3-integrin stains the plasma membrane, ClC-7 is prominently found in the ruffled border (arrowhead) and in intracellular compartments. (I) KO osteoclasts express β_3-integrin normally and are multinuclear (blue TOTO-3 staining of nuclei), but do not stain for ClC-7. (J and K) Immunofluorescent detection of H^+-ATPase. (J) WT: in some osteoclasts, the ruffled border is stained (arrowhead). (K) KO: localization at the ruffled border (arrowhead). Expression levels are similar to WT. Scale bars: (A,B,E, and F) 25 μm; (C and D) 2 μm; (G–K) 10 μm.

ClC-7 and against the osteoclast marker β_3-integrin (Figures 4H and 4I). A subset of WT osteoclasts showed ruffled border localization of ClC-7 beside an invariant intracellular staining. No ClC-7 signal was detected in C7A *Clcn7*$^{-/-}$ osteoclasts, although they always stained strongly for β_3-integrin. Labeling the DNA confirmed that also *Clcn7*$^{-/-}$ osteoclasts had multiple nuclei (Figure 4I). We also stained WT and KO bone sections for the H^+-ATPase which is highly enriched in the ruffled border of resorbing osteoclasts (Baron et al., 1985; Blair et al., 1989) (Figures 4J and 4K). Expression levels were similar, and a subset of osteoclasts of either genotype showed a prominent staining close to the bone surface.

ClC-7-Deficient Osteoclasts Are Unable to Resorb Bone In Vitro

To measure bone resorption activity in vitro, osteoclasts were isolated from the shafts of long bones from 2- to 4-day-old mice and seeded on dentine (ivory) slices. Many resorption pits were formed by WT osteoclasts, but were invariably absent from slices seeded with the same number of KO cells (data not shown). To exclude a possible defect in osteoclast maturation due to an altered environment in KO bone, we differentiated osteoclasts in vitro. Coculturing progenitor cells with ST2 stromal cells in the presence of dexamethasone and vitamin D3 yielded osteoclasts that were multinucleated, formed actin rings, and expressed TRAP irrespective of their genotypes (Figures 5A and 5B). When seeded on biotinylated ivory, WT osteoclasts were able to remove completely the biotinylated material at their attachment site (Figure 5C). This was never observed with osteoclasts differentiated from KO mice. However, some KO cells contained biotinylated material within the cytoplasm. Thus, KO osteoclasts may be able to dissolve some material from the surface initially, but cannot degrade dentin further. Osteoclasts differentiated from WT mice created many pits when seeded on ivory, whereas pits were never observed with *Clcn7*$^{-/-}$ osteoclasts (Figure 5D).

We used acridine orange fluorescence to study whether the inability of *Clcn7*$^{-/-}$ osteoclasts to degrade dentin is related to a defect in extracellular acidification. Large fluorescing orange discs were observed beneath WT, but not KO, osteoclasts (Figure 5E). *Clcn7*$^{-/-}$ osteoclasts only showed a punctate pattern of faint orange fluorescence, which corresponds to intracellular acidic compartments and which was also found in WT cells.

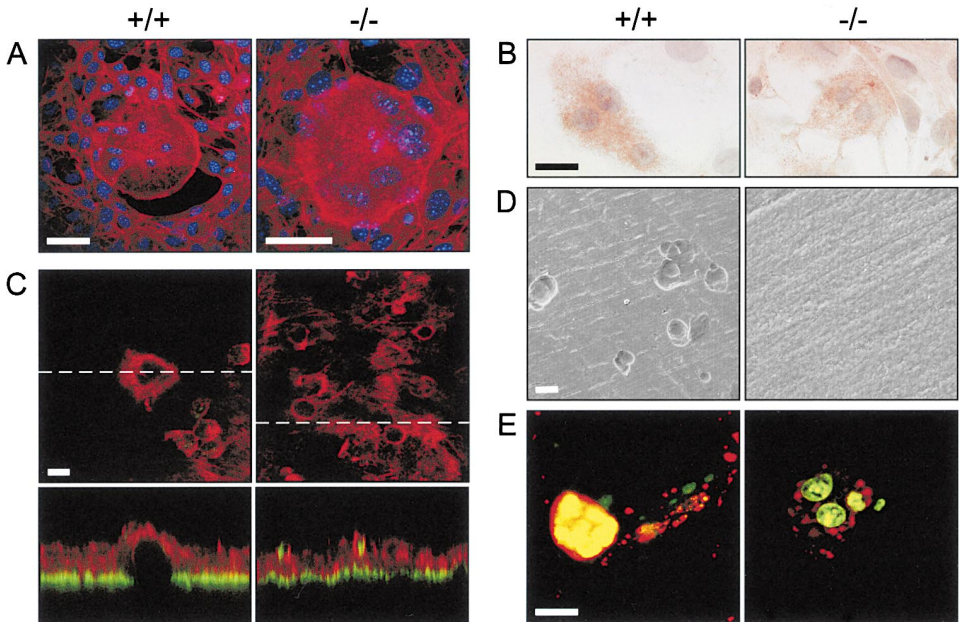

Figure 5. Properties of WT and *Clcn7*$^{-/-}$ Osteoclasts Differentiated In Vitro

(A) Both WT and KO osteoclasts differentiated in vitro formed actin rings (labeled with phalloidin Texas red) on glass. TOTO-3 iodide staining of nuclei (blue) showed that these cells have multiple nuclei. (B) Cells of both genotypes expressed the osteoclast marker TRAP (red). HE staining (blue) identified nuclei. (C) Osteoclasts after a 14 day coculture on biotinylated ivory have prominent actin rings. In the *xz*-scan (lower panel; section indicated by dotted line above), only WT osteoclasts have depleted biotin-labeled ivory components (green) from the surface. Some KO osteoclasts showed punctate intracellular green labeling, but they did not remove the surface label completely. (D) Many resorption pits are visible on ivory seeded with cocultures derived from WT, but not from KO mice. (E) Acidic compartments revealed by acridine orange. Large, fluorescent orange discs were seen in WT (left), but not in KO osteoclasts (right) on ivory. The punctate pattern corresponds to acidic intracellular vesicles. Nuclei are stained in green by acridine orange. Scale bars: (D) 20 μm; (A–C, E) 50 μm.

A similar punctate pattern was seen when cells of either genotype were stained for lamp-1 (data not shown). Thus, *Clcn7*$^{-/-}$ osteoclasts had lost the ability for extracellular acidification, but could still acidify intracellular vesicles that probably correspond to the (pre)lysosomal compartments that express ClC-7 (Figures 2G and 5K). This view is supported by a normal maturation of cathepsin D in ClC-7-deficient fibroblasts (data not shown), a process which is exquisitely sensitive to alterations of late endosomal/lysosomal pH (Gieselmann et al., 1985). We conclude that *Clcn7*$^{-/-}$ osteoclasts differentiate normally and are able to attach to bone, but fail to secrete acid although their H^+-ATPase is expressed to normal levels (Figures 4J and 4K).

Mutations in Human ClC-7 Cause Infantile Malignant Osteopetrosis

The similarity of our mouse model to the human disease prompted us to search for mutations in the *CLCN7* gene in 12 cases of infantile malignant osteopetrosis. We sequenced genomic DNA and cDNA derived from leukocytes or cultured fibroblasts obtained from these patients. One patient was compound heterozygous for a nonsense (Q555X) and a missense mutation (R762Q) in ClC-7 (Figures 6A–6C). The R762Q mutation was not found in 170 chromosomes of normal controls, excluding a polymorphism. On the cDNA level, only the missense mutation could be detected (Figure 6C). This indicated that the mRNA bearing the stop mutation is degraded, and that both mutations lie on different alleles. This is important since it was not possible to obtain DNA from the parents of the patient. R762Q abolished a positive charge within the conserved CBS2 domain (Figures 6D and 6E). To investigate whether the mutation affected protein expression, fibroblasts were analyzed by Western blotting and immunofluorescence (Figures 6F and 6G). In contrast to control cells, ClC-7 protein could not be detected in the fibroblasts from the patient.

Degeneration of the Retina and the Optic Nerve

Human malignant infantile osteopetrosis is often associated with visual impairment (Gerritsen et al., 1994). It is controversial whether this results from a compression of the optic nerve by an osteopetrotic narrowing of the optic canal, or whether there is a primary retinal degeneration. Micro-CT (computed X-ray tomography) analysis disclosed the abnormal skull shape of a P39 *Clcn7*$^{-/-}$ mouse and suggested a constriction of the optic canal (Figures 7A and 7B). Histological analysis revealed a progressive optic nerve degeneration that began at P14 (Figures 7C and 7D). There was a severe degeneration of photoreceptors (Figure 7E) that started around P15 with a shortening of their outer segments. Only a few photoreceptor nuclei remained at day P28. The number of ganglion cells, which should be affected by optic nerve compression (Berkelaar et al., 1994), were only mildly reduced at P28. This suggests that the degeneration of the optic nerve and the retina are independent events.

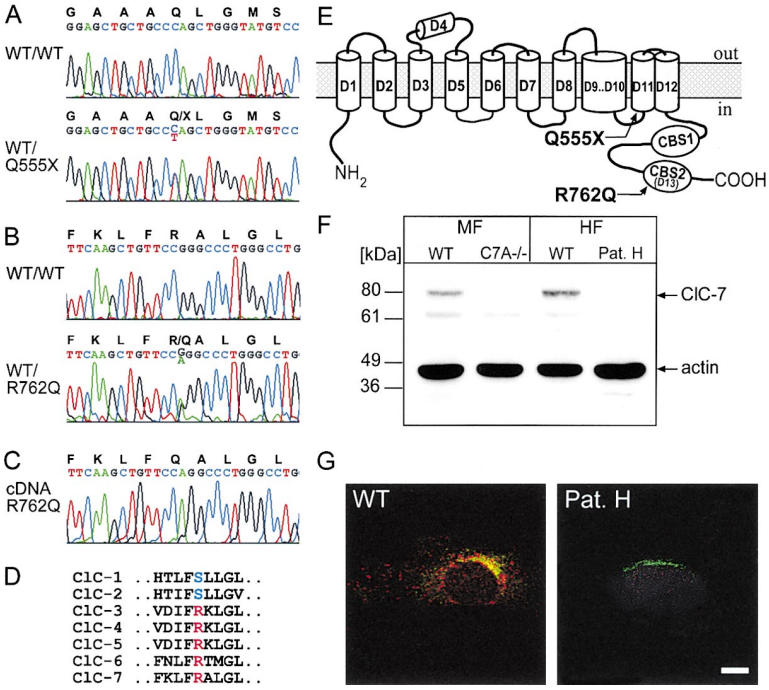

Figure 6. Sequence Analysis and Expression of ClC-7 in an Osteopetrotic Patient

(A) Genomic sequence analysis of exon 18 from patient H reveals a heterozygous stop mutation (WT/Q555X). WT/WT is a normal control. (B) Exon 24 carries a heterozygous missense mutation (WT/R762Q). (C) RT-PCR analysis of patient's fibroblast RNA detected only the allele bearing the R762Q mutation. (D) Alignment of the first part of the ClC-7 CBS2 domain with those of other CLC channels. R762 is conserved among the intracellular channels ClC-3 to -7. (E) Position of the mutations. Q555X truncates the protein within the transmembrane block, and R762Q changes a residue in the cytoplasmic domain CBS2. (F) Western blot analysis detects the ~80 kDa ClC-7 protein in both WT mouse fibroblast (MF) and human fibroblasts (HF). It was undetectable in *Clcn7*$^{-/-}$ MFs and in HFs from patient H. Actin staining confirmed equal loading. (G) Immunofluorescence analysis of ClC-7 (red) and γ-adaptin (green) in HFs. The intracellular ClC-7 staining of WT cells is absent from cells of patient H. Scale bar: 50 μm

Discussion

We have shown that ClC-7, a broadly expressed CLC chloride channel whose function has remained obscure, resides within late endosomal and lysosomal compartments. Mice deficient for ClC-7 develop severe osteopetrosis because their osteoclasts cannot secrete acid and thus cannot dissolve bone. This strongly suggests that ClC-7 provides a Cl^--conductive pathway that acts in concert with the H^+-ATPase in electroneutral hydrochloric acid transport. *Clcn7*$^{-/-}$ mice also display a severe retinal degeneration that is probably independent of an optic nerve compression. Mutations in the human *CLCN7* gene cause a similar disorder, infantile malignant osteopetrosis.

Localization and Function of ClC-7 in the Osteoclast

Although it faces the extracellular matrix, the ruffled membrane of the osteoclast is, in many respects, similar to the late endosome. Many typical markers, such as rab7, V-type H^+-ATPase, and lamp-2 are concentrated at the ruffled border (Baron et al., 1985; Palokangas et al., 1997). Moreover, the space between the ruffled membrane and the bone surface, the resorption lacuna, contains proteolytic enzymes and is highly acidic, so that this compartment is often referred to as an "extracellular lysosome." Thus, a late endosomal and lysosomal localization of ClC-7 in fibroblasts fits well with its presence in the ruffled membrane.

For bone resorption to occur, the osteoclast must be generated out of its precursors, attach to the bone surface, form the ruffled membrane, secrete acid and proteases, and remove degraded material and calcium by transcytosis (Nesbitt and Horton, 1997; Salo et al., 1997; Väänänen et al., 2000). In contrast to several other mouse models of osteopetrosis, ClC-7 deficiency does not interfere with the generation of osteoclasts or with their attachment to bone. However, *Clcn7*$^{-/-}$ osteoclasts showed functional and morphological abnormalities. They were unable to degrade bone in a pit assay, which is related to their inability to acidify the sealed extracellular space between the bone and the osteoclast. The presence of some biotinylated material within KO osteoclasts seeded on biotinylated ivory, however, suggested that some degradation was still possible. The exocytotic fusion of acidic vesicles might cause an initial, limited extracellular acidification, but the ruffled border formed by this fusion may be unable to sustain acidification due to an intrinsic secretion defect.

Ruffled membranes were poorly developed in KO osteoclasts and were reportedly absent in osteoclasts from *oc*-mice that lack an H^+-ATPase subunit (Scimeca et al., 2000). Hence, a lack of ruffled borders may correlate with a defective acidification of the resorption lacuna. Whether this is a direct effect of the pH in the lacuna on the membrane, or is rather due to a decreased exocytotic delivery of membranes into the ruffled border, remains unclear. Bone-facing areas of KO osteoclasts also contained H^+-ATPase, indicating that the biogenesis of this membrane by vesicle fusion is not entirely inhibited.

Murine Phenotype and Human Osteopetrosis

The mouse model suggested that *CLCN7* mutations may also underlie severe forms of human osteopetrosis. Indeed, 1 out of 12 osteopetrotic patients was a compound heterozygote for *CLCN7* mutations, while 9 patients had mutations in the a3 subunit of the H^+-ATPase, including patients that were described previously (Kornak et al., 2000). Thus, compared to the gene (*OC116* or *TCIRG1*) encoding the a3 subunit, *CLCN7* less often underlies malignant osteopetrosis. Microsatellite analysis and sequencing excluded mutations in either gene

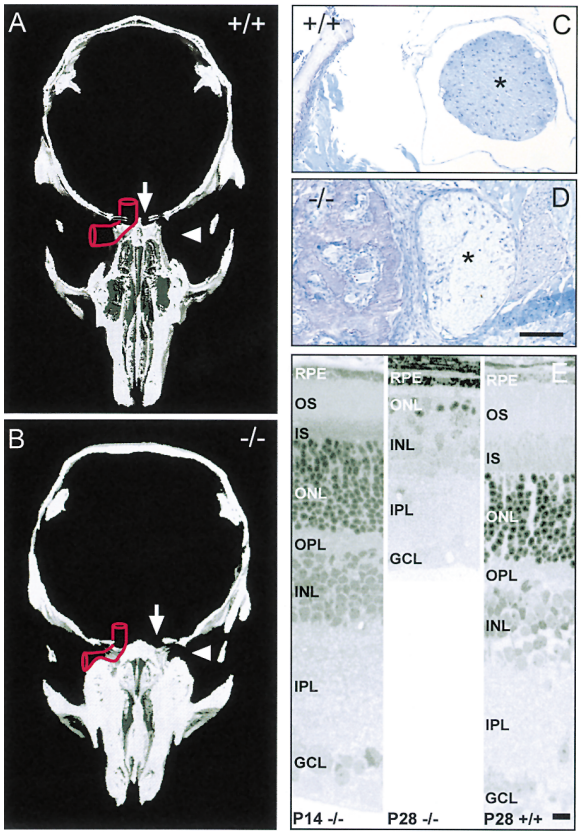

Figure 7. *Clcn7*$^{-/-}$ Mice Show a Narrowing of the Optic Canal and a Rapid Retinal Degeneration

(A and B) Horizontal Micro-CT sections of skulls at age P39. (A) WT: from the optic foramina (arrow) until the orbita (arrowhead), the optic canal (red) is wide enough to allow passage of the optic nerve. (B) KO: the optic canal (red) is narrowed behind the optic foramina and by a maxillar process. Note absence of maxillary sinus. (C and D) sections through the optic canal of WT and KO at day P39 (toluidine blue staining). (C) WT: the optic nerve (*) is not compressed. (D) KO: compression of the optic nerve (*) between two osteopetrotic bone protrusions. The nerve appears pale and degenerated. (E) Semi-thin sections of the retina. At P14, KO retina (left) still appears normal. At day P28, the degeneration of the photoreceptors in the outer nuclear layer (ONL) of the KO retina (middle) has led to an almost complete loss of photoreceptor nuclei compared to the WT control (right). Scale bars: (C and D) 100 μm ; (E) 10 μm.

in one pedigree, suggesting further genetic heterogeneity of the human disease.

It is impossible to test the impact of *CLCN7* mutations on channel function using a plasma membrane expression system. However, the truncating mutation almost certainly abolishes channel function. In addition, the premature stop codon drastically decreased the amount of mutant RNA (Culbertson, 1999). As a result, almost all ClC-7 mRNA in the patient's fibroblasts carried a missense mutation (R762Q) in the second cytoplasmic CBS (cystathionine β-synthase) domain (Ponting, 1997). The function of these domains is unknown, but mutations in CBS2 of the yeast scClC (Gef1p) led to a missorting of the protein (Schwappach et al., 1998). Moreover, a nonsense mutation at the corresponding position (R704X) in ClC-5 caused Dent's disease and abolished Cl^--currents (Lloyd et al., 1996). Most importantly, the ClC-7 protein could not be detected in the patient's fibroblasts.

Relation of Retinal Degeneration to Osteopetrosis

Visual impairment is a frequent finding in human osteopetrosis and is often attributed to optic nerve compression by a narrowing of the optic canal (Gerritsen et al., 1994). However, there are some reports of blindness in patients lacking detectable optic nerve compression. The optic canal was progressively constricted in KO mice. First signs of optic nerve degeneration were seen at P14, shortly before retinal degeneration became apparent. However, the first cells to degenerate were photoreceptors, whereas optic nerve damage initially affects ganglion cells (Berkelaar et al., 1994). This suggests that the retinal degeneration is not secondary to osteopetrosis. As ClC-7 is expressed in the neuroretina and the RPE, it is unclear whether the degeneration of photoreceptors is cell autonomous or secondary to changes in neighboring cells. Interfering with the acidification of intracellular compartments may impair the phagocytosis of photoreceptor segments by the RPE. It may also lead to a missorting of proteins or to an intracellular accumulation of material normally degraded by lysosomes. However, we found no accumulation of photoreceptor disks, nor intracellular deposits in retinal neurons as in ceroid lipofuscinoses. Interestingly, photoreceptors also degenerate in mice disrupted for ClC-3, an endosomal Cl^- channel (Stobrawa et al., 2001). Elucidating the mechanism of retinal degeneration may not be easy in either case.

The osteopetrotic patient with *CLCN7* mutations also suffered from an early visual impairment, but no retinal histology was available. A retinal pathology almost identical to the one of *Clcn7*$^{-/-}$ mice was reported in a case of infantile malignant osteopetrosis (Keith, 1968). By contrast, reports on mice lacking functional H^+-ATPase a3 subunits did not mention retinal degeneration. This may suggest that osteopetrosis associated with primary retinal degeneration is specific for *CLCN7* mutations, whereas the visual impairment in patients with defects in the H^+-ATPase might be secondary to optic nerve compression.

Molecular Diversity in Intracellular Acidification Processes

The acidification of intracellular organelles is crucial for many processes including sorting, trafficking, and luminal enzymatic activities. Most of these compartments are acidified by V-type ATPases that need a parallel Cl^--conductance for efficient pumping (al-Awqati, 1995). Given the variation in luminal pH between different organelles and the differences in trafficking and sorting events, it is not surprising that the underlying transport proteins are molecularly diverse. There is increasing evidence for different isoforms of the more than ten subunits of the V-type H^+-ATPase. Three diseases are known to be due to defects in H^+-ATPase subunits. Mutations in two different subunits result in renal tubular acidosis with and without hearing loss, respectively (Karet et al., 1999; Smith et al., 2000). Mutations in the a3 subunit cause infantile malignant osteopetrosis (Frattini et al., 2000; Kornak et al., 2000). The different pheno-

types can be explained in part by differential tissue expression. Thus, the subunits mutated in tubular acidosis are highly expressed in intercalated cells (which secrete acid after inserting the H^+-ATPase into the plasma membrane), whereas the a3 subunit is prominently, but by no means exclusively, expressed in osteoclasts (Nishi and Forgac, 2000; Toyomura et al., 2000). Despite this broad expression, mice deleted for the a3 subunit had defects in extracellular osteoclast acidification, while lysosomal pH seemed unchanged (Li et al., 1999). This may be due to the presence of other isoforms of this subunit in those compartments.

Likewise, the broadly expressed ClC-7 is essential for extracellular acidification by osteoclasts, but there was no gross effect on late-endosomal or lysosomal acidification. Probably together with other Cl^- channels, ClC-7 may be involved in acidifying late endosomes and lysosomes, but is rate limiting only for a restricted number of tissues and cells. There are several candidates for Cl^- channels that may substitute for ClC-7 in cells apparently spared by the knockout. ClC-3, -4, -5, and -6 are also intracellular channels (Günther et al., 1998; Stobrawa et al., 2001; our unpublished results). Contrasting with the late endosomal to lysosomal localization of ClC-7, ClC-3 and ClC-5 reside in earlier endocytotic compartments. It is currently unclear whether the subcellular expression of ClC-7 overlaps with any other CLC protein. CLIC proteins form a family of putative intracellular Cl^- channels, although they have just one predicted membrane span (al-Awqati, 1995). A CLIC protein, p62, was proposed to be the ruffled border Cl^- channel (Schlesinger et al., 1997). This work shows that ClC-7 is rate limiting for osteoclast acidification, but we cannot exclude an additional role of p62.

Our work has identified ClC-7 as a late endosomal to lysosomal Cl^- channel that plays a pivotal role in acidifying the extracellular lysosome between osteoclasts and the bone. Its disruption in mice and man leads to a defect in bone degradation, resulting in a severe form of osteopetrosis. We established ClC-7 as a novel player in the field of osteoclast biology, advancing our understanding of osteopetrosis and osteoporosis. The role of this ubiquitously expressed channel in other cells might be illuminated by disrupting other CLC genes together with *Clcn7*. Such studies will give further insights into the exciting roles intracellular Cl^- channels play in the function and trafficking of vesicles.

Experimental Procedures

Disruption of the *Clcn7* Gene

An ~14 kb clone containing exons 2 to 18 of *Clcn7* isolated from a 129/Sv mouse genomic library in λFixII (Stratagene) was used to generate two targeting constructs (Figure 1A). In construct C7A, exons 3 to 7 were replaced by a 1.6 kb phosphoglycerate kinase (pgk) promoter-driven neomycin (neo) resistance cassette. In construct C7B, a lacZ cDNA and a neo cassette were inserted into exon 7, deleting exons 8 to 10. Pgk promoter-driven diphtheria toxin α fragment (dta) or thymidine kinase (tk) cassettes, respectively, were fused to select against random integration. The constructs were electroporated into E14 (C7A) or R1 (C7B) ES cells. Resistant clones were analyzed by Southern blot using EcoRI and an external 1.4 kb probe. Cells from two positive clones each were injected into C57BL/6 blastocysts. Male chimeras derived from one C7A-positive clone and two C7B-positive clones were bred with C57BL/6 females. Resulting heterozygous animals were inbred to yield *Clcn7*$^{-/-}$ mice. All experiments were performed on C57BL/6-129SV mixed background. Toothless KO animals and their littermates were fed AIN-93G Liquid Diet (Dyets, Bethlehem, PA).

Micro-CT and Radiographs

Micro-CT and contact radiography used the μCT 20 (Scanco Medical) and Faxitron devices, respectively.

Generation and Characterization of ClC-7 Antibodies

Polyclonal rabbit antisera were raised against an N-terminal peptide (GRDRDDEEGAPLLC-amide) coupled to BSA through the added C-terminal cysteine. Antisera (10726 and 11753) from two different rabbits were affinity purified. Their specificity was shown by comparing WT and KO mice (Figure 1C). Both sera worked well in Western blots, but only 11753 was useful for immunohistochemistry.

Western Blot

Western blots of fibroblast lysates or cell fractions (20 μg per lane) were probed with rabbit antiserum 11753 (1:500), anti-rab4 (1:200) (Santa Cruz), or rabbit anti-actin (Sigma) (1:2000). Detection used a chemiluminescence kit (Renaissance, DuPont).

Light and Electron Microscopy

For light microscopical studies, mice were perfused with 4% paraformaldehyde (PFA) in PBS for 5 min. Undecalcified bone specimen were embedded in methacrylate, sectioned, and stained with von Kossa or toluidine blue. For immunohistochemistry, tibiae were frozen on dry ice in tissue freezing medium (Leica) and cut into 10 μm sections or decalcified, paraffin embedded, and cut into 5 μm sections. Cultured fibroblasts as well as bone sections were fixed, blocked, permeabilized, and incubated with the following antibodies: rabbit ClC-7 antiserum 11753 (1:200), rat anti-lamp-1 (1:20), mouse anti-EEA1 (1:500; Transduction Laboratories), mouse anti-protein disulfide isomerase (1:200; StressGen), mouse anti-γ-adaptin (1:500; Transduction Laboratories), mouse anti-31 kDa subunit of H^+-ATPase (obtained from S. Gluck) (1:20), and hamster anti-β3-integrin (1:200; PharMingen). The anti-lamp-1 antibody (1D4B) developed by J. T. August (Baltimore) was obtained from the Developmental Studies Hybridoma Bank (Iowa). Anti-rabbit, anti-rat, or anti-mouse IgG coupled to Alexa Fluor 488 or 546 (Molecular Probes), Cy3-conjugated goat anti-hamster (Jackson ImmunoResearch), and alkaline phosphatase- or horseradish peroxidase-coupled anti-rabbit antibodies (DAKO) were used as secondary antibodies. For retinal histology and electron microscopy, mice were perfused with 2% PFA/1% glutaraldehyde in PBS. After decalcification, tissue was postfixed in 1% OsO4, dehydrated, and embedded in Epon. Plastic sections (0.5 μm) were stained with methylene blue. Ultrathin sections (60 nm) were counterstained with uranylacetate and lead citrate and examined with a Zeiss EM 902.

X-Gal Staining of Embryos and Tibia

Day 16.5/17.5 embryos were frozen on dry ice in tissue freezing medium (Leica) and cut into 15 μm sections. Tibiae were cut longitudinally. After fixation in 4% PFA for 5 min, specimen were incubated 24 hr in PBS containing 5 mM $K_3[Fe(CN)_6]$, 5 mM $K_4[Fe(CN)_6]$, 2 mM $MgCl_2$, and 1mg/ml X-Gal at 37°C.

In Situ Hybridization

In situ hybridization with a 290 nt cRNA probe for ClC-7 representing the sequence deleted in the C7B construct was done as in Stobrawa et al. (2001).

Osteoclast Preparation and Coculture System

Authentic osteoclasts were isolated from long bones of 3-day-old mice as described in Saftig et al. (1998). To prepare osteoclasts from progenitor cells, spleen cells from 4-week-old mice were cocultured for 14 days on biotinylated ivory with ST2 stromal cells in the presence of 10 nM vitamin D_3 and 100 nM dexamethasone (Udagawa et al., 1989). Resorption pits were visualized using a Leo-435 VP scanning electron microscope (Zeiss).

Extracellular Acidification

Ivory slices seeded with osteoclasts were incubated at 37°C in Hepes-buffered MEM (pH 7.4) containing 5 μg/ml acridine orange (Molecular Probes) for 15 min, washed, and chased for 15 min (Baron et al., 1985). Analysis was by confocal microscopy using a 490 nm excitation filter and a 525 nm arrest filter (Leica TCS NT).

Subcellular Fractionation on Percoll Gradients

After 15 min in 200 mM sucrose, the MF were homogenized in 250 mM sucrose, 3 mM imidazole, pH 7.4, using a tight Douncer (30 strokes). Homogenates were centrifuged for 5 min at 1000 g, and supernatants were subjected to density gradient centrifugation on 20% Percoll (Braun et al., 1989).

RNA Isolation, Northern Blot, and RT-PCR

RNA was isolated using the RNeasy kit (Quiagen). Total RNA was reverse transcribed by Superscript RT-II (Gibco) using random hexamers. Poly(A)$^+$ RNA was purified with Dynabeads Oligo $(dT)_{25}$ (DYNAL), electrophoresed, and blotted following standard protocols. A 3′-terminal fragment of rat ClC-7 served as probe.

Analysis of DNA and RNA from Patient with Infantile Malignant Osteopetrosis

Patient H was the only child of unaffected nonconsanguineous parents. No other cases of the disease were known in the family of either parent. After initial normal postnatal development, growth retardation became apparent after two weeks, followed by symptoms of anemia. Histological and radiographic signs of osteopetrosis were present. DNA was prepared from cultured fibroblasts from a skin biopsy. All 25 exons of the *CLCN7* gene were amplified using intronic primers deduced from sequence AL031600 (GenBank). ClC-7 cDNA was amplified from fibroblast cDNA. PCR products were sequenced on ABI 377 or ABI 310 sequencers (Applied Biosystems). To detect 2285G>A (R762Q), we amplified exon 24 and digested the 352 bp PCR product with AlwNI, yielding a 225 and a 127 bp fragment for the mutant allele.

Acknowledgments

We thank G. Weets and P. Hausmann for technical assistance, S. Fehr for in situ hybridizations, C. Gentzsch for scanning electron microscopy, E. Plüger for help with lacZ staining, E. Lissel for mouse photography, S. Gluck for proton pump antibodies, and the Hamburg Customs for compounding tusks from African elephants. This work was supported by the DFG, the Fonds der Chemischen Industrie, and the Louis-Jeantet Prize for Medicine to T. J. J., and by the DFG to G. D.

Received October 24, 2000; revised December 21, 2000.

References

al-Awqati, Q. (1995). Chloride channels of intracellular organelles. Curr. Opin. Cell Biol. *7*, 504–508.

Baron, R., Neff, L., Louvard, D., and Courtoy, P.J. (1985). Cell-mediated extracellular acidification and bone resorption: evidence for a low pH in resorbing lacunae and localization of a 100-kD lysosomal membrane protein at the osteoclast ruffled border. J. Cell Biol. *101*, 2210–2222.

Berkelaar, M., Clarke, D.B., Wang, Y.C., Bray, G.M., and Aguayo, A.J. (1994). Axotomy results in delayed death and apoptosis of retinal ganglion cells in adult rats. J. Neurosci. *14*, 4368–4374.

Blair, H.C., Teitelbaum, S.L., Ghiselli, R., and Gluck, S. (1989). Osteoclastic bone resorption by a polarized vacuolar proton pump. Science *245*, 855–857.

Brandt, S., and Jentsch, T.J. (1995). ClC-6 and ClC-7 are two novel broadly expressed members of the CLC chloride channel family. FEBS Lett. *377*, 15–20.

Braun, M., Waheed, A., and von Figura, K. (1989). Lysosomal acid phosphatase is transported to lysosomes via the cell surface. EMBO J. *8*, 3633–3640.

Christenson, R.H. (1997). Biochemical markers of bone metabolism: an overview. Clin. Biochem. *30*, 573–593.

Culbertson, M.R. (1999). RNA surveillance. Unforeseen consequences for gene expression, inherited genetic disorders and cancer. Trends Genet. *15*, 74–80.

Frattini, A., Orchard, P.J., Sobacchi, C., Giliani, S., Abinun, M., Mattsson, J.P., Keeling, D.J., Andersson, A.K., Wallbrandt, P., Zecca, L., et al. (2000). Defects in TCIRG1 subunit of the vacuolar proton pump are responsible for a subset of human autosomal recessive osteopetrosis. Nat. Genet. *25*, 343–346.

Gaxiola, R.A., Yuan, D.S., Klausner, R.D., and Fink, G.R. (1998). The yeast CLC chloride channel functions in cation homeostasis. Proc. Natl. Acad. Sci. USA *95*, 4046–4050.

Gerritsen, E.J., Vossen, J.M., van Loo, I.H., Hermans, J., Helfrich, M.H., Griscelli, C., and Fischer, A. (1994). Autosomal recessive osteopetrosis: variability of findings at diagnosis and during the natural course. Pediatrics *93*, 247–253.

Gieselmann, V., Hasilik, A., and von Figura, K. (1985). Processing of human cathepsin D in lysosomes in vitro. J. Biol. Chem. *260*, 3215–3220.

Greene, J.R., Brown, N.H., DiDomenico, B.J., Kaplan, J., and Eide, D.J. (1993). The *GEF1* gene of Saccharomyces cerevisiae encodes an integral membrane protein; mutations in which have effects on respiration and iron- limited growth. Mol. Gen. Genet. *241*, 542–553.

Günther, W., Lüchow, A., Cluzeaud, F., Vandewalle, A., and Jentsch, T.J. (1998). ClC-5, the chloride channel mutated in Dent's disease, colocalizes with the proton pump in endocytotically active kidney cells. Proc. Natl. Acad. Sci. USA *95*, 8075–8080.

Jentsch, T.J., Friedrich, T., Schriever, A., and Yamada, H. (1999). The CLC chloride channel family. Pflügers Arch. *437*, 783–795.

Karet, F.E., Finberg, K.E., Nelson, R.D., Nayir, A., Mocan, H., Sanjad, S.A., Rodriguez-Soriano, J., Santos, F., Cremers, C.W., Di Pietro, A., et al. (1999). Mutations in the gene encoding B1 subunit of H^+-ATPase cause renal tubular acidosis with sensorineural deafness. Nat. Genet. *21*, 84–90.

Keith, C.G. (1968). Retinal atrophy in osteopetrosis. Arch. Ophthalmol. *79*, 234–241.

Kornak, U., Bösl, M.R., and Kubisch, C. (1999). Complete genomic structure of the *CLCN6* and *CLCN7* putative chloride channel genes. Biochim. Biophys. Acta *1447*, 100–106.

Kornak, U., Schulz, A., Friedrich, W., Uhlhaas, S., Kremens, B., Voit, T., Hasan, C., Bode, U., Jentsch, T.J., and Kubisch, C. (2000). Mutations in the a3 subunit of the vacuolar H^+-ATPase cause infantile malignant osteopetrosis. Hum. Mol. Genet. *9*, 2059–2063.

Lazner, F., Gowen, M., Pavasovic, D., and Kola, I. (1999). Osteopetrosis and osteoporosis: two sides of the same coin. Hum. Mol. Genet. *8*, 1839–1846.

Li, Y.P., Chen, W., Liang, Y., Li, E., and Stashenko, P. (1999). *Atp6i*-deficient mice exhibit severe osteopetrosis due to loss of osteoclast-mediated extracellular acidification. Nat. Genet. *23*, 447–451.

Lloyd, S.E., Pearce, S.H., Fisher, S.E., Steinmeyer, K., Schwappach, B., Scheinman, S.J., Harding, B., Bolino, A., Devoto, M., Goodyer, P., et al. (1996). A common molecular basis for three inherited kidney stone diseases. Nature *379*, 445–449.

Nesbitt, S.A., and Horton, M.A. (1997). Trafficking of matrix collagens through bone-resorbing osteoclasts. Science *276*, 266–269.

Nishi, T., and Forgac, M. (2000). Molecular cloning and expression of three isoforms of the 100-kDa a subunit of the mouse vacuolar proton-translocating ATPase. J. Biol. Chem. *275*, 6824–6830.

Palokangas, H., Mulari, M., and Väänänen, H.K. (1997). Endocytic pathway from the basal plasma membrane to the ruffled border membrane in bone-resorbing osteoclasts. J. Cell Sci. *110*, 1767–1780.

Piwon, N., Günther, W., Schwake, M., Bösl, M.R., and Jentsch, T.J. (2000). ClC-5 Cl^--channel disruption impairs endocytosis in a mouse model for Dent's disease. Nature *408*, 369–373.

Ponting, C.P. (1997). CBS domains in ClC chloride channels implicated in myotonia and nephrolithiasis (kidney stones). J. Mol. Med. *75*, 160–163.

Saftig, P., Hunziker, E., Wehmeyer, O., Jones, S., Boyde, A., Rommerskirch, W., Moritz, J.D., Schu, P., and von Figura, K. (1998). Impaired osteoclastic bone resorption leads to osteopetrosis in cathepsin-K-deficient mice. Proc. Natl. Acad. Sci. USA *95*, 13453–13458.

Salo, J., Lehenkari, P., Mulari, M., Metsikko, K., and Väänänen, H.K. (1997). Removal of osteoclast bone resorption products by transcytosis. Science *276*, 270–273.

Schlesinger, P.H., Blair, H.C., Teitelbaum, S.L., and Edwards, J.C. (1997). Characterization of the osteoclast ruffled border chloride channel and its role in bone resorption. J. Biol. Chem. *272*, 18636–18643.

Schwappach, B., Stobrawa, S., Hechenberger, M., Steinmeyer, K., and Jentsch, T.J. (1998). Golgi localization and functionally important domains in the NH_2 and COOH terminus of the yeast CLC putative chloride channel Gef1p. J. Biol. Chem. *273*, 15110–15118.

Scimeca, J.C., Franchi, A., Trojani, C., Parrinello, H., Grosgeorge, J., Robert, C., Jaillon, O., Poirier, C., Gaudray, P., and Carle, G.F. (2000). The gene encoding the mouse homologue of the human osteoclast-specific 116-kDa V-ATPase subunit bears a deletion in osteosclerotic (oc/oc) mutants. Bone *26*, 207–213.

Simon, D.B., Bindra, R.S., Mansfield, T.A., Nelson-Williams, C., Mendonca, E., Stone, R., Schurman, S., Nayir, A., Alpay, H., Bakkaloglu, A., et al. (1997). Mutations in the chloride channel gene, *CLCNKB*, cause Bartter's syndrome type III. Nat. Genet. *17*, 171–178.

Sly, W.S., Hewett-Emmett, D., Whyte, M.P., Yu, Y.S., and Tashian, R.E. (1983). Carbonic anhydrase II deficiency identified as the primary defect in the autosomal recessive syndrome of osteopetrosis with renal tubular acidosis and cerebral calcification. Proc. Natl. Acad. Sci. USA *80*, 2752–2756.

Smith, A.N., Skaug, J., Choate, K.A., Nayir, A., Bakkaloglu, A., Ozen, S., Hulton, S.A., Sanjad, S.A., Al-Sabban, E.A., Lifton, R.P., et al. (2000). Mutations in ATP6N1B, encoding a new kidney vacuolar proton pump 116-kD subunit, cause recessive distal renal tubular acidosis with preserved hearing. Nat. Genet. *26*, 71–75.

Steinmeyer, K., Klocke, R., Ortland, C., Gronemeier, M., Jockusch, H., Gründer, S., and Jentsch, T.J. (1991). Inactivation of muscle chloride channel by transposon insertion in myotonic mice. Nature *354*, 304–308.

Stobrawa, S.M., Breiderhoff, T., Takamori, S., Engel, D., Schweizer, M., Zdebik, A.A., Bösl, M.R., Ruether, K., Jahn, H., Draguhn, A., et al. (2001). Disruption of ClC-3, a chloride channel expressed on synaptic vesicles, leads to a loss of the hippocampus. Neuron *29*, 185–196.

Toyomura, T., Oka, T., Yamaguchi, C., Wada, Y., and Futai, M. (2000). Three subunit a isoforms of mouse vacuolar H^+-ATPase. Preferential expression of the a3 isoform during osteoclast differentiation. J. Biol. Chem. *275*, 8760–8765.

Udagawa, N., Takahashi, N., Akatsu, T., Sasaki, T., Yamaguchi, A., Kodama, H., Martin, T.J., and Suda, T. (1989). The bone marrow-derived stromal cell lines MC3T3–G2/PA6 and ST2 support osteoclast-like cell differentiation in cocultures with mouse spleen cells. Endocrinology *125*, 1805–1813.

Väänänen, H.K., Zhao, H., Mulari, M., and Halleen, J.M. (2000). The cell biology of osteoclast function. J. Cell Sci. *113*, 377–381.